

מכון ויצמן למדע

WEIZMANN INSTITUTE OF SCIENCE



## Brain investigations of rodent disease models by chemical exchange saturation transfer at 21.1T

### Document Version:

Accepted author manuscript (peer-reviewed)

### Citation for published version:

Roussel, T, Rosenberg, JT, Grant, SC & Frydman, L 2018, 'Brain investigations of rodent disease models by chemical exchange saturation transfer at 21.1T', *NMR in Biomedicine*, vol. 31, no. 11, e3995.  
<https://doi.org/10.1002/nbm.3995>

*Total number of authors:*

4

### Digital Object Identifier (DOI):

[10.1002/nbm.3995](https://doi.org/10.1002/nbm.3995)

### Published In:

NMR in Biomedicine

### License:

Unspecified

### General rights

@ 2020 This manuscript version is made available under the above license via The Weizmann Institute of Science Open Access Collection is retained by the author(s) and / or other copyright owners and it is a condition of accessing these publications that users recognize and abide by the legal requirements associated with these rights.

### How does open access to this work benefit you?

Let us know @ [library@weizmann.ac.il](mailto:library@weizmann.ac.il)

### Take down policy

The Weizmann Institute of Science has made every reasonable effort to ensure that Weizmann Institute of Science content complies with copyright restrictions. If you believe that the public display of this file breaches copyright please contact [library@weizmann.ac.il](mailto:library@weizmann.ac.il) providing details, and we will remove access to the work immediately and investigate your claim.

# Brain investigations of rodent disease models by chemical exchange saturation-transfer at 21.1 T

Tangi Roussel,<sup>1</sup> Jens T. Rosenberg,<sup>2</sup> Samuel C. Grant<sup>2,3</sup> and Lucio Frydman<sup>1,2</sup>

[1] Department of Chemical and Biological Physics, Weizmann Institute of Science, 76100 Rehovot, Israel

[2] National High Magnetic Field Laboratory, Tallahassee, FL 32310, United States

[3] Department of Chemical & Biomedical Engineering, The Florida State University, Tallahassee, FL 32313, United States

**E-mail addresses:** [tangi.roussel@weizmann.ac.il](mailto:tangi.roussel@weizmann.ac.il), [rosenberg@magnet.fsu.edu](mailto:rosenberg@magnet.fsu.edu), [grant@magnet.fsu.edu](mailto:grant@magnet.fsu.edu), [lucio.frydman@weizmann.ac.il](mailto:lucio.frydman@weizmann.ac.il)

**Number of text words:** 5623 in the main text; 213 in abstract; 128 in the Supporting Information

**Number of figures:** 8 in main text; 2 in the Supporting Information

**Number of tables:** 0

**Number of references:** 58 in the main text

**Conflicts of Interest:** None

**Running title (<50 characters not incl. spaces):** Brain disorders characterized by 21.1T CEST MRI

**Abbreviations:** APT, amide proton transfer; CEST, chemical exchange saturation transfer; FLASH, fast low angle shot; LFD, Lorentzian fit difference; MCAO, middle cerebral artery occlusion; MT, magnetization transfer;  $MTR_{\text{asym}}$ , magnetization transfer ratio asymmetry; NOE, nuclear Overhauser effect; RARE, rapid acquisition with relaxation enhancement; RF, radio-frequency; SAR, specific absorption rate; TE, echo time; TR, repetition time; ROI, region of interest; WASSR, water saturation shift referencing.

## Abstract

This study explores opportunities opened by ultrahigh fields for *in vivo* saturation-transfer brain MRI experiments. Fast spin-echo images weighted by chemical-exchange saturation-transfer effects were collected on Sprague Dawley rats at 21.1 T, focusing on two neurological models. One involved a middle cerebral artery occlusion emulating ischemic stroke; the other involved xenografted glioma cells that were followed over the course of several days as they developed into brain tumors. A remarkably strong saturation-derived contrast was observed for the growing tumors when calculating magnetization transfer ratios at ca. 3.8 ppm. This large contrast originated partially from an increase in the contribution of the amide chemical exchange saturation-transfer effect, but mostly from strong decreases in the Overhauser and magnetization transfer contributions to the upfield region, whose differential attenuations could be clearly discerned thanks to the ultrahigh field. The high spectral separation arising at 21.1 T also revealed numerous CEST signals usually overlapping at lower fields. Ischemic lesions were also investigated but, remarkably, magnetization- and saturation-transfer contrasts were nearly absent when computing transfer asymmetries using either high or low saturation power schemes. These behaviors were consistently observed 24 hs post-occlusion, regardless of the data processing approach assayed. Considerations related to how various parameters defining these experiments depend on magnetic field, primarily chemical shifts and  $T_1$ s, are discussed.

**Keywords:** ischemic stroke; brain glioma; chemical exchange saturation transfer; ultrahigh field MRI; magnetization transfer.

## Introduction

Saturation transfer is a well-known effect in magnetic resonance, exploited in analytical spectroscopic contexts for several decades.<sup>1</sup> These phenomena have become widely used also in biological settings with the advent of chemical exchange saturation transfer (CEST) and magnetization transfer (MT) measurements. Endogenous contrast mechanisms that arise when selectively irradiating peaks associate to either labile hydrogens or to other sites that can eventually lead to changes in the water signal intensity.<sup>1-7</sup> CEST in particular highlights molecules carrying labile hydrogens, including fundamental metabolites such as creatine, glucose, glutamate and urea.<sup>8-11</sup> Chemical exchanges between these species and water can be determined by recording so-called Z-spectra, multi-scan experiments where the effect on the water peak is monitored upon applying presaturating radiofrequency (RF) pulses irradiating at an array of offsets. While this frequency-selective saturation procedure forfeits the possibility of interrogating all the labile hydrogens simultaneously, this is compensated by the potential amplification of the site specific information afforded by CEST. In the slow exchange regime, this amplification will be on the order of  $k_{ex}T_1^{water}$ —where  $k_{ex}$  is the rate of solvent exchange of the labile hydrogen and  $T_1^{water}$  is the relaxation time of the solvent.<sup>2,6,7</sup> In favorable cases this magnification can reach  $\approx 100$ -1000, leading to the possibility of using CEST as an *in vivo* metabolic imaging tool. The most prominent CEST peaks do not usually arise in either healthy or tumorous brain tissues from metabolites but rather from amide groups and aliphatic sidechains in proteins, or from other macromolecular components.<sup>12-14</sup> The reduction in the water signal intensity arising when saturating endogenous contrast sources positioned 3.5 ppm downfield from water is usually referred to as the amide proton transfer (APT) contribution to CEST MRI. Z-spectra also often reveal water saturation upon irradiating upfield of the water resonance, in a region where no labile protons resonate. This effect is usually assigned to the saturation of lipid end groups or of protein sidechains that, via direct cross-relaxation with structural water molecules or via cross-relaxation with protons in amides or in hydroxyls that then exchange with H<sub>2</sub>O, result in partial saturation of the bulk water peak. Regardless of the exact transfer pathway, these are known as nuclear Overhauser effect (NOE) contributions.<sup>15,16</sup> Finally, besides these relatively narrow dips arising upon saturating specific species, changes in the water signal intensity may arise *in vivo* when irradiating over a much larger range of frequency offsets—as far as 10 ppm away from the water resonance. These changes originate from the saturation of protons in semi-solid macromolecules, whose dipolar-broadened lines can be subject to couplings in the tens of kHz. When irradiating this homogeneously broadened background, saturation can be transferred to the free water resonance via cross-relaxation or even by direct dipolar coupling with structural water molecules at a rate  $k_{MT}$ ; as these free up and become “normal”, liquid-like water molecules, the dominating water signal intensity drops. This forms the basis of the magnetization transfer (MT) contrast, which is often considered as a phenomenon akin to—but distinct from—CEST. Besides all these information-carrying contributions there may also be contribution to the Z-spectrum associated to changes that the water peak itself experiences when performing off-resonance irradiation. These contributions to the water’s peak saturation will incorporate a variety of relative relaxation ( $T_1$ ,  $T_2$ ,  $T_2^*$ ) and RF ( $B_1$ ) factors. In order to deal with these “spillover effects”, it is customary to compute both CEST- and MT-derived images by performing two experiments

where saturation is symmetrically placed around the water resonance. It is then the relative difference between these two effects, known as the magnetization transfer ratio asymmetry  $MTR_{asym}(\Delta\omega)$ , which is usually reported in these experiments. Further corrections may have to be introduced to account for shifts in the water resonance position within the targeted region-of-interest (ROI).<sup>17</sup> To disentangle all these competing and simultaneous mechanisms that can contribute to the  $MTR_{asym}$  an increasing number of sophisticated signal processing approaches have been proposed, including quantitative techniques based on single or multi-Lorentzian fitting models, and on Bloch equation calculations.<sup>16,18-21</sup>

Z-spectra and images deriving from CEST and MT effects depend on physiologically valuable parameters including metabolic concentrations, temperature and pH.<sup>12,14,22,23</sup> They also depend on parameters that are metabolically less meaningful but spectroscopically important, including the solvent's access to and exchange with the protons of macromolecules and metabolites, as well as the latter's species spin relaxation properties. A particularly important variable in defining the nature of CEST and MT parameters is the magnetic field strength  $B_0$ . Besides the well-known enhancements in sensitivity and in resolution arising upon increasing  $B_0$ , higher fields will separate the frequency differences  $\Delta\nu$  (in Hz) between the exchanging species and water. This will in turn expand the range of processes that can contribute to the CEST/MT observations, and whose rates  $k_{ex}$ ,  $k_{MT}$  need to be on the order of  $\Delta\nu$  (or smaller) in order to enable a substantial magnification of the targeted resonances. In complex systems such as living tissues, these  $k$ 's will normally entail a heterogeneous distribution of frequencies; increasing  $\Delta\nu$  by moving to higher fields thus increases the range of participating processes, augmenting the experiment's contrast.<sup>21</sup> Furthermore, as field increases, water –which although a small molecule interacts strongly with its surrounding environment– will lengthen its  $T_1$  with  $B_0$ .<sup>24,25</sup> The overall  $kT_1^{water}$  product defining MT/CEST's maximum amplification is thus expected to increase with the operating field  $B_0$ . Such behavior has been observed in preliminary paramagnetic and diamagnetic CEST measurements<sup>26,27</sup> and recently reported in a preclinical field-comparative study,<sup>28</sup> suggesting that the use of ultrahigh fields could open hitherto untapped contrasting possibilities. The present study explores this hypothesis, by applying CEST imaging methodologies to examine brain-related conditions on rats at 21.1 T. The two conditions chosen were glioma and stroke, diseases that have been extensively used to study injuries to brain's white and gray matters by CEST MRI in the past.<sup>12-15,29-37</sup> In those studies an  $MTR_{asym}$  increase of approximately 2 to 10% was observed at ca. +3.5 ppm, upon comparing glioma with healthy brain tissue.<sup>13,29-32,35,37,38</sup> Moreover, since chemical exchange rates of amides depend on the tissue micro-environment,<sup>4,14,15</sup> APT-derived CEST weighting has been proposed as an imaging method to quantify pH and from there to detect brain strokes.<sup>12</sup> In this study an intense  $MTR_{asym}$  contrast was observed at 21.1 T on glioma rat tissues, considerably larger than that hitherto observed at lower fields. Several processing methods were used to identify and quantify the various contributions to this enhanced  $MTR_{asym}$ . By contrast, the changes in  $MTR_{asym}$  did not reach statistical significance in the stroke cases, providing much weaker reporters than  $T_2$  or diffusion observables when examined 24 hs post-stroke. Potential explanations for these features and prospects of additional ultrahigh magnetic field studies in these brain investigations, are discussed.

## Experimental Methods

**Animal handling:** All surgical procedures were carried out under aseptic conditions in accordance with the guidelines for animal experimentation from the ethical committee of the Florida State University Animal Care and Use Committee. FSU is registered as a research facility with the United States Department of Agriculture (USDA Registration #58-R-0001) and has an Animal Welfare Assurance number (#A3854-01) on file with the US Public Health Service. All animal procedures were undertaken according to these regulatory bodies and AAALAC guidelines, under the direction of a veterinarian who is certified as a specialist in laboratory animal medicine by the American College of Laboratory Animal Medicine (ACLAM). Naïve Sprague Dawley rats were purchased from Envigo Corp. (Tampa, FL, USA) and delivered one week prior to surgery for acclimatization to the new environment. All animals were housed individually in a 12 hr night/12 hr daylight cycle with water and food available ad libitum. For each disease model, male Sprague-Dawley rats weighing between 200-250 gr were randomly chosen from the cohort of available animals. Seven animals were chosen to provide statistical significance results by means of power analysis, while at the same time minimize the number of animals used. After an aseptical preparation, the surgical site was infiltrated with 0.2 mL of 0.5% Bupivacaine (Hospira, Lake Forest, IL). In addition, 0.05 mg/kg of buprenorphine (Reckitt Benckiser Pharmaceuticals, Inc.) was injected subcutaneously and every 4-6 hour or as needed for pain management. After surgery, all animals were given pre-warmed fluids (3-5 mL 1X PBS) intraperitoneally to facilitate recovery. Animals were let to recover in a pre-warmed (37°C) recovery cage. Euthanasia was performed in guidance with the 2007 American Veterinary Medical Association (AVMA) Guidelines on Euthanasia. After the last MRI session animals were anesthetized with isoflurane and exposed to CO<sub>2</sub> for a fast and pain free euthanasia. Once respiratory failure and cardiac arrest had occurred, a cervical dislocation was performed.

**Ischemic animal model:** Seven juvenile male Sprague-Dawley rats were anesthetized with 5% isoflurane (Baxter, Deerfield, IL) in an induction chamber and maintained on 3-4% isoflurane during the surgical procedure. After administration of a local nerve block (Bupivacaine), the common carotid artery, external carotid artery and internal carotid artery were exposed by blunt and sharp dissection. A 3.0-cm filament with a 0.35-mm thick and 2-3 mm long rubber coating (Doccol Corp, Redlands, CA, USA) was inserted through the ECA. The filament was guided 1.9 cm into the ICA or until the middle carotid artery (MCA) was blocked. The transient occlusion occurred for 1.5 h, followed by re-anesthetization and removal of the filament. The animals were imaged 24 h following the occlusion; no mortalities were documented during the course of the experiments.

**Glioma animal model:** 9L glioma cells were cultured and expanded in 75 cm<sup>3</sup> tissue culture flasks with Dulbeccos modified Eagle's medium (DMEM) (Sigma Chemical Co. St Louis, MO) supplemented with 10% fetal bovine serum (Atlanta Biological, Atlanta, GA, USA), 1% antibiotics/antimycotics (Gibco, Invitrogen Corp., Carlsbad, CA, USA) and 0.1% gentamycin (Invitrogen Corp., Carlsbad, CA, USA). Cells were kept at a temperature of 37 °C and under 5% CO<sub>2</sub>. Immediately before implantation surgery, cells were harvested with trypsin (Gibco, Invitrogen Corp., Carlsbad, CA, USA), pelleted by centrifugation, and re-suspended in phosphate buffered saline (PBS). For intra-cranial implantation, eleven Sprague-Dawley rats were used. Animals

anesthetized with isoflurane were secured in a stereotaxic frame with continuous flow of 2-3% Isoflurane. A 1-cm mid-line incision was made over the skull and the dermal tissues were kept separated by bull clamps. Using the bregma as reference, a 1-mm burr hole was made 2 mm anterior and 2.5 mm lateral. Using a sterile Hamilton syringe (SigmaAldrich, St Louis, MO), 100,000 9L glioma rat cells in 10  $\mu$ L of sterile PBS were injected at depth of 3.5 mm from the skull. Immediately after the removal of the syringe, bone wax was used to seal the burr hole and 70% ethanol applied to the skull to prevent any cells from forming exogenous tumors. The incision was then sealed with sutures. Animals were imaged 7 and 11 days following implantation. Two rats died between days 7 and 11.

**CEST MRI acquisitions:** All data were acquired using the 105-mm bore, 21.1 T (900 MHz) vertical magnet available at the National High Magnetic Field Laboratory MRI/MRS user facility in Tallahassee, FL, USA.<sup>39</sup> The magnet is equipped with a Bruker Avance III console running on Paravision<sup>®</sup> 5.1 (Bruker Biospin, Billerica, MA), and imaging gradients (Resonance Research Inc., Billerica, MA) delivering a peak strength of 600 mT/m with rise times of 120  $\mu$ s. A custom-built transmit/receive quadrature double saddle surface coil was used in these <sup>1</sup>H MR experiments, whose performance –including B<sub>1</sub> specifications– has been recently described.<sup>40</sup> The coil is part of a probe equipped with a bite-bar supplying continuous flow of anesthesia and provisions to maintain animals at a constant temperature. Prior to their *in vivo* imaging all animals were anesthetized with 5% Isoflurane; this was then lowered to 2% and adjusted to maintain a respiratory rate between 30-40 breaths/min as monitored with a pneumatic pillow situated under the animal (SA Instruments Inc., Stony Brook, NY). Scout fast low angle shot images (FLASH, TE/TR=4/50 ms) were collected to help with the animal positioning; this was followed by CEST-weighted <sup>1</sup>H rapid acquisition with relaxation enhancement (RARE) spin-echo (SE) images, collected with echo and recycling times of TE/TR=9/5000 ms. As CEST-based MRI is an intrinsically time consuming experiment, its ability to generate neurological contrast for the aforementioned models was studied at 21.1 T in two experimental stages. One of this involved a low resolution, fast protocol; the second was a lengthier protocol with high spatial and spectral resolution plus inhomogeneity corrections, aimed at better defining the possibilities of CEST at this field.

*Fast, low-resolution CEST MRI:* Five MCAO animals and six glioma-bearing animals were scanned using a fast, low-resolution CEST MRI protocol. These images were acquired from a 32x32-mm<sup>2</sup> field of view, using a 1-mm slice thickness and a 250x250  $\mu$ m<sup>2</sup> in-plane resolution. The CEST preparation module consisted of a train of 400 10-ms Gaussian pulses with a B<sub>1</sub> field of 3.5  $\mu$ T, each of them followed by a low intensity spoiler gradient. To obtain full Z-spectra, the frequency offset of the saturating pulse train was varied between –10 and +10 ppm relative to water, with a 1-ppm increment step between  $\pm$ 10 and  $\pm$ 4 ppm and a 0.5-ppm step between -4 and +4 ppm (23 increments in total). The total scan time for this CEST MRI protocol was ca. 30 minutes.

*High resolution CEST MRI:* Two MCAO and five glioma-bearing animals were scanned using a high spectral resolution CEST MRI protocol. These images were acquired from a 32x32-mm<sup>2</sup> field of view, using a 1-mm slice thickness and a 200x200  $\mu$ m<sup>2</sup> in-plane resolution. The CEST preparation module consisted of a train of 400 10-ms Gaussian pulses with a B<sub>1</sub> field of 1.5  $\mu$ T, with the frequency offset of these pulses varied between –5 and +5 ppm relative to water in 0.2-

ppm steps (56 increments). CEST images were also recorded at  $\pm 100$ ,  $\pm 20$  and  $\pm 10$  ppm in order to establish the wider Z-spectral contributions during quantification. Water saturation shift referencing (WASSR) maps<sup>17</sup> were also acquired for these experiments, and their impact on the CEST data when attempting to correct for water frequency shifts was assessed. These WASSR preparation modules consisted of a single 200-ms long saturation Gaussian pulse with a  $B_1$  of  $0.5 \mu\text{T}$ , and frequency offsets varying from  $-0.3$  to  $+0.3$  ppm with a  $0.05$ -ppm step (13 increments). In order to check the field homogeneity and the RF transmission performance,  $B_0$  and  $B_1$  maps were acquired using, respectively, a 3D phase imaging sequence (Fieldmap,  $128 \times 128$  matrix) and a saturated double-angle method.<sup>41</sup> The total scan time for this CEST MRI protocol was ca. 3 hours.

**Data processing:** CEST/MT-weighted images were processed and quantified using a customized MATLAB<sup>®</sup> (The Mathworks Inc, Nantucket, MA) code. This quantification involved computing

$$MTR_{asym}(D\omega) = \frac{S(-D\omega) - S(+D\omega)}{S_0} \times 100$$

$MTR_{asym}$  maps, generated as  $MTR_{asym}(D\omega) = \frac{S(-D\omega) - S(+D\omega)}{S_0} \times 100$ , where  $S(\pm\Delta\omega)$  reflect the water signal intensity upon irradiating at two frequencies symmetrically placed with respect to the water, and  $S_0$  is a water reference signal acquired when the saturation frequency is far off-resonance ( $+100$  ppm in this study). With  $MTR_{asym}$  maps obtained in this manner the rat brain images were manually segmented, and two ROIs were selected highlighting either normal or diseased (ischemic or glioma) brain tissues. For each animal, the optimal saturation frequency  $\Delta\omega$  yielding the highest  $MTR_{asym}$  contrast between normal and diseased tissues was estimated, and employed for later statistical use. WASSR maps were generated using a spline interpolation and  $MTR_{asym}$  maps were calculated with and without  $B_0$  correction. A Lorentzian fit difference (LFD) processing<sup>20</sup> was also applied to each voxel in the analysis of their corresponding Z-spectra. The purpose of the LFD was to extract CEST components after suppressing the direct water saturation (spillover) effects, and the procedure was performed in two steps. First, an automatic fitting procedure adjusted the amplitude and damping parameters of a double-Lorentzian model centered on  $0$  ppm using a least-squares optimization method; subsequently, the residual of this double-Lorentzian fit was extracted to reveal any residual CEST components disturbing the symmetry of a pure water Z-spectrum. Upfield and downfield CEST contributions were also quantified using another method: the so-called three-offset technique.<sup>15,34</sup> Here the Z-spectrum is linearly interpolating between two *a priori* chosen frequency offsets of interest (for instance two offsets  $1$  ppm apart), and then a search is made for the maximum difference between this fitted line and the original spectrum, so as to reveal the offset and amplitude of any CEST component potentially present. APT/NOE contributions were quantified in these two fashions between frequency offsets of  $+2/+4$  ppm and  $-2/-5$  ppm respectively, and quantitative APT/NOE maps were thus generated. Other spectral contributions centered at  $+2$  and  $1.8$  ppm were quantified using  $[+1.6;+2.4]$  and  $[-2;-1.5]$  ppm chemical shift ranges.

**Statistical Analysis:** Quantitative measures were averaged over the indicated ROIs and are presented with  $\pm$  standard deviation of the mean. Statistical significance was determined with students T-test with significance set at the p-values indicated in the text.

## Results

Figure 1 shows representative  $T_2$ -weighted,  $B_1$  and WASSR maps obtained on an MCAO animal at 21.1 T. The quadrature double saddle surface coil used in these experiments<sup>40</sup> is able to generate a relatively homogeneous  $B_1$  coverage of the rat brain, with only slight drops in power in the lower and peripheral parts. Similarly,  $B_0$  field homogeneity was excellent in the upper and central parts of the brain, as evidenced by the WASSR maps. In general, the largest frequency shifts were evidenced in the lower parts of the brain, likely originating distortions imposed by proximity to the nose and to the ear canals, compounded by low SNR due to the surface coil sensitivity profile and.

Figures 2-4 summarize various features observed when CEST experiments were carried out on glioma-bearing animals. The maps in Figures 2 and 3 illustrate axial RARE results acquired for different Z-spectral offsets, for a glioma-implanted rat at days 7 and 11 post-injection of the cancerous cells, and for two different saturation conditions. Notice for all cases the intensification and the expansion of the contrast in the right hemisphere, as the tumor develops. Interestingly, similar contrasts between normal brain and glioma-invaded tissues are observed under low and high  $B_1$  CEST conditions. Nevertheless, the low  $B_1$  experiments allowed the observation of spectrally selective CEST effects, by reducing the sensitivity to the broad MT effects otherwise observable up to 10 ppm. Figure 4 offers a description of this, with the  $MTR_{asym}$  contrast displayed by glioma tissue when recorded (on a different animal) using the high-resolution CEST imaging protocol. Shown in panel (a) are anatomical  $T_2$ -weighted images, which themselves show only a weak contrast stemming from the tumor. Figure 4b are the Z-spectral data observed as a function of frequency, when integrated over ROIs associated with healthy (green) and diseased (red) tissues. The large differential CEST changes are highlighted by the  $MTR_{asym}$  spectrum, as this results from subtracting contributions on opposite sides of the water resonance (Fig. 4c). The CEST  $MTR_{asym}$  maps shown in Figure 4d illustrate how, upon choosing the most intense asymmetry offset, the tumor can be clearly distinguished from healthy tissue at both stages (similar maps are presented for additional  $MTR_{asym}$  offsets in Figure 2). When considered over the  $n=5$  animal cohort studied under the low-power conditions, the maximum  $MTR_{asym}$  contrast for glioma tissue was statistically observed at  $4.0 \pm 0.5$  ppm for the day-7 time point, and at  $3.7 \pm 0.1$  ppm for the day-11 time point. For those offsets, the average changes in  $MTR_{asym}$  between normal and glioma brain tissue were, respectively,  $6.2 \pm 1.9$  % and  $7.3 \pm 1.5$  %.

Figure 5 shows an alternative way of processing these CEST data. These images show quantitative maps obtained for different irradiation frequencies, upon using the LFD method on data acquired from a rat bearing a 7-day glioma. As reminder, this Lorentzian deconvolution is done to remove the effects of direct water saturation as well as potentially also magnetization transfer effects (though the latter are relatively weak under the low  $B_1$  conditions pertaining these data); the residual highlights all remaining, physiologically relevant mechanisms acting as main sources of contrast. A weak contrast is then observed upon saturating at ca. -3.5 ppm, in the region normally associated with aliphatic resonances, and a positive contrast appears at +3.5 ppm, in the region normally associated with labile hydrogens and APT effects. Notice that this is opposite to the trend shown by the localized Z-spectra illustrated in Figure 4, which revealed a strong decrease in

$MTR_{asym}$  contrast's absolute value for the cancerous tissues. Figure 5b gives a different rendering of these changes and illustrates, after averaging over normal and diseased brain ROIs for the full animal cohort studied at  $B_1=1.5 \mu T$ , the Z-spectra arising for different chemical shifts after subtracting the water/MT spillover contributions. These LFD results highlight the APT increase associated to the glioma. The signal processing approach, in combination with the high-resolution Z-spectrum acquisition conditions, then shows to a number of finer Z-spectral features at these 21.1T field. These include downfield CEST contributions usually ascribed mostly to intrinsic protein constituents: amides at +3.5 ppm, side-chain amines at +2.5 ppm,<sup>42</sup> creatine plus other amines usually assigned to the +2 ppm peak (although this has also been tentatively connected by MAS NMR cross relaxation experiments to aromatic sidechains<sup>43</sup>), and a novel feature arising at +4.6 ppm. The spectral LFD deconvolution of the upfield NOE hump also reveals a fine structure, including a -1.8 ppm NOE-mediated peak that has been associated to choline head groups,<sup>44</sup> and peaks at -3.0, -3.5 and -3.8 ppm that have been related to macromolecular methylene and methyl protons.<sup>45</sup>

Figure 6 shows a further evaluation of these results for the  $n=5$  animal cohort in the low-power glioma study, this time quantifying the CEST behavior based on the “three-offsets” technique reported by Gore and coworkers.<sup>34</sup> This approach also successfully identifies the eight peaks noted in Figure 5; out of all these Figure 6 focuses solely on the four peaks where potentially significant changes were seen upon focusing on ROIs containing healthy and glioma-bearing tissues. This quantification evidenced a positive change in intensity when considering the APT region between normal brain and day-11 glioma tissue (Fig. 6a,  $p<0.1$ ). More significant NOE changes were evidenced by the upfield part of the spectrum (Fig. 6b), with a -1.3% decrease ( $p<0.05$ ) between normal brain and day-7 glioma tissue and a -1.4% decrease ( $p<0.05$ ) in the case of day-11 glioma tissues. The amines component at +2 ppm and the minor NOE component at -1.8 ppm also showed significant changes ( $p<0.1$ ), between normal brain and day-11 glioma tissue (Fig. 6c and 6d).

It is interesting to contrast these glioma data, which are mutually consistent regardless of the adopted data-processing approach, against 21.1 T results observed when the pathology is associated with a MCAO-derived ischemia. Figure 7 shows how this event, clearly seen in the anatomical images of the stroked animals when investigated 24 hs after the injury, fails to reveal a particular chemical shift for which a significant  $MTR_{asym}$  is evidenced under the low-power, high-resolution CEST conditions used in the glioma studies. This is further illustrated by the Z-spectral images shown in Figure 8, where the dominant direct water saturation was subtracted using the LFD method. Some contrast features are evident by these residuals, but these do not correspond to the stroked regions. This absence that does not mean that the Z spectra are identical for healthy and stroked regions: in general, we observe under these conditions a slight decrease of a spectrally broad effect on the latter (e.g., Fig. 7). These could reflect different MT behaviors, but also differences in the water relaxation characteristics (and thereby in the spillover and the saturation-transfer effects) between healthy and diseased tissues. Moreover, unlike in the glioma case, the asymmetry of these saturation-transfer plots about the water is not significantly distorted upon going from one kind of tissue to the other. As illustrated in the Supporting Information, a similar behavior is observed when examining MCAO animals 24 hs post-occlusion, under high-power ( $B_1$

= 3.5 $\mu$ T) saturating conditions. This robs the 21.1T  $MTR_{asym}$  plots from contrast capabilities: over the  $n=5$  cohort that we analyzed using the low-resolution / high  $B_1$  CEST imaging protocol and the  $n=2$  cohort analyzed at high-resolution / low  $B_1$ , no significant change ( $p>0.5$ ) in either APT or NOE regions could be quantified for the ischemic tissues.

## Discussion and Conclusions

Multiple physical factors suggest that saturation-based contrasts in MRI should benefit from operating at the highest possible fields. The range of chemical exchange rates accessible in this manner would increase due to a larger chemical shift dispersion expanding in turn the NMR timescales, while water's lengthening *in vivo*  $T_{1S}$ <sup>24,25,46</sup> mean that the imprint of the saturation onto the bulk water pool could also be increased.<sup>19,21,42,47</sup> The relation between  $B_0$  strength and CEST, however, is not straightforward. As mentioned, larger CEST effects have been observed for glucose and other agents at 21.1 T than at lower fields;<sup>26,27</sup> NOE and MT effects have also been reported to increase for human gliomas with increasing fields.<sup>37</sup> The present 21.1 T study is in agreement with this latter trend, as for both healthy and glioma tissues, enhancements are observable. Subtler, however, is the extraction of systematic conclusions about how these saturation processes depend on field. Thus, while remarkable  $MTR_{asym}$  contrasts were observed at either high or low presaturation powers for the glioma,  $MTR_{asym}$  effects were always ambiguous for ischemia—a lesion that at this field could be much more robustly detected at these fields with standard  $T_2$ -weighted images or by diffusion measurements.<sup>48</sup>

The strong contrast observed at 21.1 T when comparing tumor versus normal brain tissues, can be traced to an increase in the downfield chemical exchange effects and to a decrease in the upfield NOE and magnetization transfer effects. APT increases in brain tumors have been reported at lower fields in animals (4.7 and 9.4 T<sup>13,29,34,35</sup>) and in humans (3 and 7 T<sup>30,37,38</sup>), with the enhancements ranging between +1 and +4%. Interestingly, we were not able to compute a significant correlation between the APT contrasts reported in the literature and the employed  $B_0$  fields. This is not entirely unexpected since, apart from similar  $MTR_{asym}$  values, the reported APT contrasts present in the literature are very heterogeneous and were obtained with different acquisition protocols and of APT quantification approaches—thus preventing quantitative comparative studies. Still, and in agreement with literature trends, a significant ( $p<0.1$ ) +0.2% APT increase was observed when comparing normal brain to day-11 glioma tissues. The changes in the upfield saturation has been less clearly established for glioma tissue, and only at high preclinical (9.4 T) or clinical fields (7 T) have decreases in CEST effects ranging between -1 and -2%, been reported for this NOE component—depending on the quantification tool.<sup>31,32,34,37,38,49</sup> In agreement with these reports, a -1.3 to -1.4% decrease was observed in the extent of the upfield saturation peak at 21.1 T, which together with the increase in the APT CEST contributed to an  $MTR_{asym}$  contrast amounting to ca. -6.2% when focusing at ca. +4.0 ppm under lower-power saturation conditions (Fig. 4c). An even larger,  $\geq|5\%|$  drop is observed in the upfield saturation when operating under high-power conditions, which together with the APT increase leads to an  $MTR_{asym}$  contrast amounting to  $\approx -15\%$  when focusing at ca. +3.3 ppm (Fig. 3). This is, to our knowledge, the largest contrast hitherto observed by CEST on

gliomas. The sizable drop in MT under these conditions is observable at chemical shifts far away from water –as distant as -10 ppm. Recent works have suggested that glioma’s rise in APT may be related to an increased protein content in tumors,<sup>50</sup> a claim that remains to be backed by biochemical measurements of total protein contents in normal and malignant brains.<sup>34</sup> Alternatively, the rise in APT could reflect a change in intracellular pH that increases the rate of proton exchange, or the onset of protein unfolding facilitating amide exchanges with water.<sup>14,51</sup> As for the drop observed in the upfield NOE response, this could also be related to structural changes, including protein unfolding or progressive cellular membrane fracture.<sup>16</sup> In any case, out of all the effects, it is the drop in MT that yields the main source of contrast between healthy and glioma tissues –an effect that, although to very different extents, happens regardless of whether a low or high  $B_1$  saturation power is used (see Supplementary Information for examples of the latter). MT originates from “immobile” protons present in proteins, macromolecules or lipids, and exhibits a maximum effect ca. -2 ppm upfield from the  $H_2O$  resonance.<sup>7,52</sup> The MT drop observed in the strong- $B_1$ , 21.1 T experiments is in agreement with recent results observed in 9L rat glioma tissue at 9.4 T,<sup>34</sup> even if the increased frequency separation and the longer water  $T_1$  in the field here used probably enhances this change. Whereas such broad and baseline CEST signals strongly compromise the asymmetry analysis when attempting to estimate APT and NOE contributions, the LFD and the three-offsets quantification methods are not sensitive to this effect and provide a solid high-field observable that can highlight the progress of the disease. The exact reasons behind this MT reduction remain to be defined, but it would be reasonable to link them to a degradation of the structural tissue integrity, to an onset of necrosis, and to an increase in water content as the glioma grows.<sup>53</sup>

The presence and changes in the dominant MT contribution compromises the estimation of the finer APT and NOE contributions, particularly when attempting an  $MTR_{asym}$  analysis at high  $B_1$  fields. The deconvolution that the LFD and the three-offsets quantification methods carry out, however, provide reliable observables that can disentangle CEST peaks under moderate  $B_1$  conditions. The use of a high Z-spectral resolution coupled with the spectral separation power arising at 21.1 T, reveal in this manner APT and NOE contributions at -3.8, -3.0, -1.8, +2.0, +2.6, +3.5 and +4.6 ppm away from the water peak. The two upfield components at -3.8 and -3.0 ppm are usually associated to protein and/or membrane methyl and methylenes, and they did not show significant variations between healthy and diseased tissues. Zhang *et al*<sup>44</sup> reported a NOE-mediated signal around -1.6 ppm in ischemic rats at 9.4 T, which we believe corresponds to the -1.8 ppm peak observed here. This peak was tentatively assigned to choline phospholipids; while Zhang *et al* saw a minor decrease in this peak in their stroke study, the 21.1 T Z-spectra revealed an increase in day-11 glioma compared to normal brain tissues for this peak (Fig. 6d). By contrast, no statistically significant change was observed for this peak in the MCAO rats (Figs. 7 and 8). The labile amine sites of creatine and protein guanidino amine groups at ca +2 ppm<sup>55,56</sup> show a slight but significant drop in the glioma cases (Fig. 6c), in agreement with the literature reporting a decrease in 9L tumors in rats.<sup>54</sup> A slight increase is observed in tumorous tissues for the +3.5ppm peak (Fig. 6c), which could reflect the onset of protein unfolding and concurrent solvent exposure for the amide peaks. This is also as previously observed at lower fields.<sup>54</sup> Finally, a low intensity but significantly

glioma-increased CEST signal was detected at +4.6 ppm relative to water. To our knowledge no reports of endogenous CEST agents for such chemical shifts are available; a potential source for this peak could be nicotinamide, which has chemical shifts ranging between 8.6 and 9.6 ppm. And while  $\text{NAD}^+$  concentrations in brain are extremely low ( $\approx 500 \mu\text{mol/L}$ ), de Graaf et al were able to detect this metabolite *in vivo* using a non-water suppressed MRS sequence thanks to its substantial exchange with the solvent.<sup>57</sup>

By contrast to these marked healthy-vs-tumor tissue effects, saturation-transfer imaging at 21.1 T provided poor contrast when applied to the ischemic rat model (Figs. 7 and 8). Previous CEST imaging studies suggest a decrease in APT of +1 to +3% in ischemic brain tissue,<sup>12,14,15,36,44</sup> reflecting perhaps the acidic environment induced by the ischemia. On the other hand NOE is reported to remain nearly unchanged by ischemia.<sup>44</sup> The present study revealed differences between ischemic and normal Z spectra, but no statistically significant  $MTR_{asym}$  of LFD peaks emerging at 21.1 T. Indeed, most of the visual differences arising in Figure 7 between normal and ischemic tissues, were erased in the images shown in Figure 8 after deconvolving the direct and MT saturation components. Interestingly, a slight narrowing of the Z-spectra acquired in ischemic tissues can be observed; this could originate from a number of factors including changes in the relaxation properties of water (as visible on the  $T_2$ -weighted images) or from more complex mechanisms involving a pH-modulation of both APT and NOE effects.<sup>58</sup> All our measurements were done once, at 24h post MCAO; since ischemia is supposed to exhibit a fast temporal evolution, it remains to see whether these CEST measurements and their lack of contrast at 21.1T, would vary with time.<sup>36</sup> Regardless of this, these stroke measurements suggest that the more favorable chemical shift dispersion and longer water  $T_1$  characteristically provided by ultrahigh field operation, do not always translate into unambiguously stronger CEST peaks.

In summary, CEST methods were applied at 21.1 T to investigate the contrasts arising for two widely investigated neurological disorders. Both of these had been investigated previously in human and rodent models at lower fields; when repeated at ultrahigh fields at low and high  $B_1$  saturation fields, strong endogenous saturation-transfer contrasts resulted for MRI of gliomas. The origins of these could be traced to changes in the APT and NOE contributions to CEST, as well as on MT effects originating from the solid-like tissue matrices. Interestingly, the use of ultrahigh field in combination with relatively low powers and with high resolution Z-spectral conditions, successfully resolved in both healthy and glioma brain regions multiple CEST signals usually entangled at lower fields. New, potentially useful endogenous markers for glioma were also identified in this manner. By contrast, poor  $MTR_{asym}$  changes could be observed for ischemic tissues under similar conditions, a limitation whose exact origin is still under examination.

**Acknowledgements.** The authors thank Mr. Ashley Blue, Ms. Shannon Helsper and Dr. Ali Darkazalli (FSU) for technical and surgical assistance and Prof. Cathy Levenson (FSU) for providing the 9L-glioma cells and helpful insights to the glioma animal model. This work was performed at the National High Magnetic Field Laboratory (NHMFL), which is supported by NSF DMR-1157490, NSF DMR-1644779 and the State of Florida. Funding was also provided by the NHMFL User Collaboration Group Program and by the American Heart Association Grant-In-aid program (10GRNT3860040) (to SCG). The authors also thank the Israel Science Foundation

(ISF/NSFC grant 2508/17), the EU through ERC-2016-PoC grant # 751106, the Helen and Martin Kimmel Institute of Magnetic Resonance (Weizmann Institute) and the generosity of the Perlman Family Foundation (to LF).

## References

1. Wolff SD, Balaban RS. Magnetization transfer contrast (MTC) and tissue water proton relaxation in vivo. *Magn Reson Med* 1989; 10:135-144.
2. Lemaire L, Franconi F, Saint-Andre JP, Roullin VG, Jallet P, Le Jeune JJ. High-field quantitative transverse relaxation time, magnetization transfer and apparent water diffusion in experimental rat brain tumour. *NMR Biomed* 2000; 13:116-123.
3. Ward KM, Aletras AH, Balaban RS. A new class of contrast agents for MRI based on proton chemical exchange dependent saturation transfer (CEST). *J Magn Res* 2000; 143:79-.
4. Ward KM, Balaban RS. Determination of pH using water protons and chemical exchange dependent saturation transfer (CEST). *Magn Reson Med* 2000; 44:799-802 doi: .
5. Vinogradov E, Sherry AD, Lenkinski RE. CEST: from basic principles to applications, challenges and opportunities. *J Magn Reson* 2013; 229:155-172 doi: 10.1016/j.jmr.2012.11.024.
6. Zaiss M, Bachert P. Chemical exchange saturation transfer (CEST) and MR Z-spectroscopy in vivo: a review of theoretical approaches and methods. *Phys Med Biol* 2013; 58:R221-R269 doi: 10.1088/0031-9155/58/22/R221.
7. McMahon MT, Gilad AA, Bulte JW, van Zijl PC. *Chemical Exchange Saturation Transfer Imaging: Advances and Applications*. Pan Stanford; 2017. 496 p.
8. Dagher AP, Aletras A, Choyke P, Balaban RS. Imaging of urea using chemical exchange-dependent saturation transfer at 1.5T. *J Magn Reson Imaging* 2000; 12:745-748 doi: .
9. Cai K, Haris M, Singh A et al. Magnetic resonance imaging of glutamate. *Nat Med* 2012; 18:302-306 doi: 10.1038/nm.2615.
10. Walker-Samuel S, Ramasawmy R, Torrealdea F et al. In vivo imaging of glucose uptake and metabolism in tumors. *Nat Med* 2013; 19:1067-1072 doi: 10.1038/nm.3252.
11. Haris M, Singh A, Cai K et al. A technique for in vivo mapping of myocardial creatine kinase metabolism. *Nat Med* 2014; 20:209-214 doi: 10.1038/nm.3436.
12. McVicar N, Li AX, Gonçalves DF et al. Quantitative tissue pH measurement during cerebral ischemia using amine and amide concentration-independent detection (AACID) with MRI. *J Cereb Blood Flow Metab* 2014; 34:690-698 doi: 10.1038/jcbfm.2014.12.
13. Zhou J, Lal B, Wilson DA, Larterra J, van Zijl PCM. Amide proton transfer (APT) contrast for imaging of brain tumors. *Magn Reson Med* 2003; 50:1120-1126 doi: 10.1002/mrm.10651.
14. Zhou J, Payen J-F, Wilson DA, Traystman RJ, van Zijl PCM. Using the amide proton signals of intracellular proteins and peptides to detect pH effects in MRI. *Nat Med* 2003; 9:1085-1090 doi: 10.1038/nm907.
15. Jin T, Wang P, Zong X, Kim S-G. MR imaging of the amide-proton transfer effect and the pH-insensitive nuclear overhauser effect at 9.4 T. *Magn Reson Med* 2013; 69:760-770 doi: 10.1002/mrm.24315.
16. Lu J, Zhou J, Cai C, Cai S, Chen Z. Observation of true and pseudo NOE signals using CEST-MRI and CEST-MRS sequences with and without lipid suppression. *Magn Reson Med* 2015; 73:1615-1622 doi: 10.1002/mrm.25277.

17. Kim M, Gillen J, Landman BA, Zhou J, van Zijl PCM. Water saturation shift referencing (WASSR) for chemical exchange saturation transfer (CEST) experiments. *Magn Reson Med* 2009; 61:1441-1450 doi: 10.1002/mrm.21873.
18. Liu D, Zhou J, Xue R, Zuo Z, An J, Wang DJJ. Quantitative characterization of nuclear overhauser enhancement and amide proton transfer effects in the human brain at 7 Tesla. *Magn Reson Med* 2013; 70:1070-1081 doi: 10.1002/mrm.24560.
19. McMahon MT, Gilad AA, Zhou J, Sun PZ, Bulte JWM, van Zijl PCM. Quantifying exchange rates in chemical exchange saturation transfer agents using the saturation time and saturation power dependencies of the magnetization transfer effect on the magnetic resonance imaging signal (QUEST and QUESP): Ph calibration for poly-L-lysine and a starburst dendrimer. *Magn Reson Med* 2006; 55:836-847 doi: 10.1002/mrm.20818.
20. Zaiss M, Schmitt B, Bachert P. Quantitative separation of CEST effect from magnetization transfer and spillover effects by Lorentzian-line-fit analysis of z-spectra. *J Magn Res* 2011; 211:149-155 doi: 10.1016/j.jmr.2011.05.001.
21. van Zijl PCM, Yadav NN. Chemical exchange saturation transfer (CEST): what is in a name and what isn't?. *Magn Reson Med* 2011; 65:927-948 doi: 10.1002/mrm.22761.
22. Delli Castelli D, Ferrauto G, Cutrin JC, Terreno E, Aime S. In vivo maps of extracellular pH in murine melanoma by CEST-MRI. *Magn Reson Med* 2014; 71:326-332 doi: 10.1002/mrm.24664.
23. Longo DL, Bartoli A, Consolino L et al. In Vivo Imaging of Tumor Metabolism and Acidosis by Combining PET and MRI-CEST pH Imaging. *Cancer Res* 2016; 76:6463-6470 doi: 10.1158/0008-5472.CAN-16-0825.
24. Rooney WD, Johnson G, Li X et al. Magnetic field and tissue dependencies of human brain longitudinal  $^1\text{H}_2\text{O}$  relaxation in vivo. *Magn Reson Med* 2007; 57:308-318 doi: 10.1002/mrm.21122.
25. Shemesh N, Rosenberg JT, Dumez J-N, Grant SC, Frydman L. Metabolic T1 dynamics and longitudinal relaxation enhancement in vivo at ultrahigh magnetic fields on ischemia. *J Cereb Blood Flow Metab* 2014; 34:1810-1817 doi: 10.1038/jcbfm.2014.149.
26. Cornell HH, Grant SC, Rosenberg JT et al. Characterization of Paramagnetic Lanthanide Ion complexes as MRI Contrast Agents as a Function of Magnetic Field Strength. In 15th Joint Annual International Society for Magnetic Resonance in Medicine Conference, Berlin, Germany, pp. 861.
27. Markovic S, Rosenberg J, Hespeler S et al. Maternal and fetal glucose uptake followed by chemical exchange saturation transfer imaging (glucoCEST) on pregnant mice at 21.1 T. In 25th Joint Annual International Society for Magnetic Resonance in Medicine Conference, Honolulu, HI, USA, pp. 1031.
28. Chung JJ, Choi W, Jin T, Lee JH, Kim S-G. Chemical-exchange-sensitive MRI of amide, amine and NOE at 9.4 T versus 15.2 T. *NMR Biomed* 2017; doi: 10.1002/nbm.3740.
29. Salhotra A, Lal B, Laterra J, Sun PZ, van Zijl PCM, Zhou J. Amide proton transfer imaging of 9L gliosarcoma and human glioblastoma xenografts. *NMR Biomed* 2008; 21:489-497 doi: 10.1002/nbm.1216.
30. Zhou J, Blakeley JO, Hua J et al. Practical data acquisition method for human brain tumor amide proton transfer (APT) imaging. *Magn Reson Med* 2008; 60:842-849 doi: 10.1002/mrm.21712.

31. Jones CK, Huang A, Xu J et al. Nuclear Overhauser enhancement (NOE) imaging in the human brain at 7T. *Neuroimage* 2013; 77:114-124 doi: 10.1016/j.neuroimage.2013.03.047.
32. Zaiss M, Kunz P, Goerke S, Radbruch A, Bachert P. MR imaging of protein folding in vitro employing nuclear-Overhauser-mediated saturation transfer. *NMR Biomed* 2013; 26:1815-1822 doi: 10.1002/nbm.3021.
33. Sagiya K, Mashimo T, Togao O et al. In vivo chemical exchange saturation transfer imaging allows early detection of a therapeutic response in glioblastoma. *Proc Natl Acad Sci U S A* 2014; 111:4542-4547 doi: 10.1073/pnas.1323855111.
34. Xu J, Zaiss M, Zu Z et al. On the origins of chemical exchange saturation transfer (CEST) contrast in tumors at 9.4 T. *NMR Biomed* 2014; 27:406-416 doi: 10.1002/nbm.3075.
35. Heo H-Y, Zhang Y, Lee D-H, Hong X, Zhou J. Quantitative assessment of amide proton transfer (APT) and nuclear overhauser enhancement (NOE) imaging with extrapolated semi-solid magnetization transfer reference (EMR) signals: Application to a rat glioma model at 4.7 Tesla. *Magn Reson Med* 2015; doi: 10.1002/mrm.25581.
36. Li H, Zu Z, Zaiss M et al. Imaging of amide proton transfer and nuclear Overhauser enhancement in ischemic stroke with corrections for competing effects. *NMR Biomed* 2015; 28:200-209 doi: 10.1002/nbm.3243.
37. Zaiss M, Windschuh J, Goerke S et al. Downfield-NOE-suppressed amide-CEST-MRI at 7 Tesla provides a unique contrast in human glioblastoma *Magn Reson Med* 2016; doi: 10.1002/mrm.26100.
38. Zaiss M, Windschuh J, Paech D et al. Relaxation-compensated CEST-MRI of the human brain at 7T: Unbiased insight into NOE and amide signal changes in human glioblastoma. *Neuroimage* 2015; 112:180-188 doi: 10.1016/j.neuroimage.2015.02.040.
39. Markiewicz WD, Brey WW, Cross TA et al. A Decade of Experience With the UltraWide-Bore 900-MHz NMR Magnet *IEEE J. Adv. Supercon.* 2015; 25:1-5.
40. Rosenberg JT, Shemesh N, Muniz JA, Dumez J-N, Frydman L, Grant SC. Transverse relaxation of selectively excited metabolites in stroke at 21.1 T. *Magn Reson Med* 2017; 77:520-528 doi: 10.1002/mrm.26132.
41. Cunningham CH, Pauly JM, Nayak KS. Saturated double-angle method for rapid B1+ mapping. *Magn Reson Med* 2006; 55:1326-1333 doi: 10.1002/mrm.20896.
42. Desmond KL, Moosvi F, Stanis GJ. Mapping of amide, amine, and aliphatic peaks in the CEST spectra of murine xenografts at 7 T. *Magn Reson Med* 2014; 71:1841-1853 doi: 10.1002/mrm.24822.
43. Chen J-H, Sambol EB, Decarolis P et al. High-resolution MAS NMR spectroscopy detection of the spin magnetization exchange by cross-relaxation and chemical exchange in intact cell lines and human tissue specimens. *Magn Res Med* 2006; 55:1246-1256 doi: 10.1002/mrm.20889.
44. Zhang X-Y, Wang F, Afzal A et al. A new NOE-mediated MT signal at around -1.6ppm for detecting ischemic stroke in rat brain. *Magn Reson Imaging* 2016; 34:1100-1106 doi: 10.1016/j.mri.2016.05.002.
45. Behar KL, Ogino T. Characterization of macromolecule resonances in the <sup>1</sup>H NMR spectrum of rat brain. *Magn Reson Med* 1993; 30:38-44.
46. Dobre MC, Uğurbil K, Marjanska M. Determination of blood longitudinal relaxation time (T1) at high magnetic field strengths. *Magn Reson Imaging* 2007; 25:733-735 doi:

10.1016/j.mri.2006.10.020.

47. Henkelman RM, Stanisz GJ, Graham SJ. Magnetization transfer in MRI: a review. *NMR Biomed* 2001; 14:57-64 doi: 10.1002/nbm.683.

48. Leftin A, Rosenberg JT, Solomon E, Bejarano FC, Grant SC, Frydman L. Ultrafast in vivo diffusion imaging of stroke at 21.1 T by spatiotemporal encoding *Magn Reson Med* 2015; 73:1483-1489 doi: 10.1002/mrm.25271.

49. Paech D, Burth S, Windschuh J et al. Nuclear Overhauser Enhancement imaging of glioblastoma at 7 Tesla: region specific correlation with apparent diffusion coefficient and histology. *PLoS One* 2015; 10:e0121220 doi: 10.1371/journal.pone.0121220.

50. Yan K, Fu Z, Yang C et al. Assessing Amide Proton Transfer (APT) MRI Contrast Origins in 9 L Gliosarcoma in the Rat Brain Using Proteomic Analysis. *Molecular imaging and biology: The official publication of the Academy of Molecular Imaging* 2015; 17:479-487 doi: 10.1007/s11307-015-0828-6.

51. Wen Z, Hu S, Huang F et al. MR imaging of high-grade brain tumors using endogenous protein and peptide-based contrast. *Neuroimage* 2010; 51:616-622 doi: 10.1016/j.neuroimage.2010.02.050.

52. Swanson S, Pang Y. MT is Symmetric but Shifted with Respect to Water. In 11th Annual International Society for Magnetic Resonance in Medicine Conference, Toronto, Canada, pp. 660.

53. Upadhyay N, Waldman AD. Conventional MRI evaluation of gliomas. *British J Radiol* 2011; 84 Spec No 2:S107-S111 doi: 10.1259/bjr/65711810.

54. Cai K, Singh A, Poptani H et al. CEST signal at 2ppm (CEST@2ppm) from Z-spectral fitting correlates with creatine distribution in brain tumor *NMR Biomed* 2014; doi: 10.1002/nbm.3216.

55. Zhang XY, Xie J, Wang F et al. Assignment of the molecular origins of CEST signals at 2 ppm in rat brain. *Magn Reson Med* 2017; 78:881-887 doi: 10.1002/mrm.26802.

56. Chen L, Zeng H, Xu X et al. Investigation of the contribution of total creatine to the CEST Z-spectrum of brain using a knockout mouse model. *NMR Biomed* 2017; 30:e3834 doi: 10.1002/nbm.3834.

57. de Graaf RA, Behar KL. Detection of cerebral NAD(+) by in vivo <sup>1</sup>H NMR spectroscopy. *NMR Biomed* 2014; 27:802-809 doi: 10.1002/nbm.3121.

58. Heo HY, Zhang Y, Burton TM et al. Improving the detection sensitivity of pH-weighted amide proton transfer MRI in acute stroke patients using extrapolated semisolid magnetization transfer reference signals. *Magn Reson Med* 2017; 78:871-880 doi: 10.1002/mrm.26799.

## Figure Captions

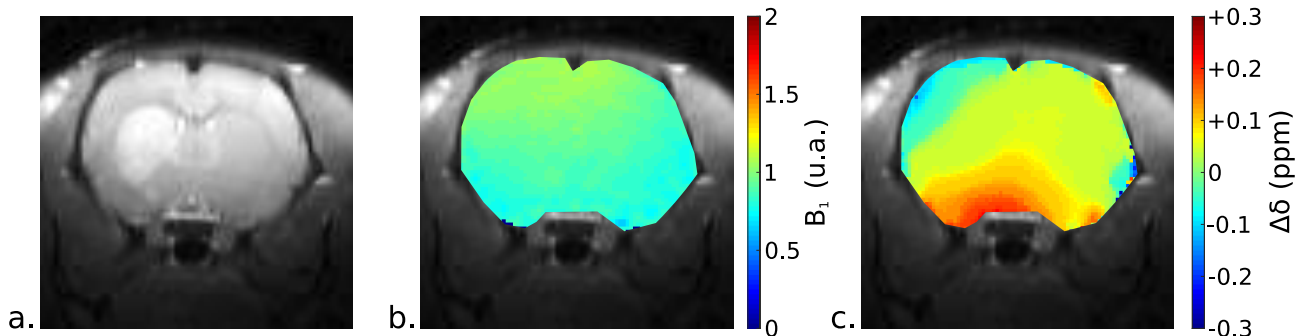


**Figure 1:** Representative T<sub>2</sub>-weighted RARE image (a), B<sub>1</sub> map (b) and WASSR map (c) acquired on an MCAO rat at 21.1 T. The ischemic tissue is clearly visible in the left hemisphere of the brain on the T<sub>2</sub>-weighted image. The B<sub>1</sub> map shows a general homogeneity over the brain with a slight over-tipping effect near the coil (top of the brain) whereas the WASSR map reveals an overall high B<sub>0</sub> homogeneity with  $\approx 0.15$  ppm heterogeneities in the lower brain regions.

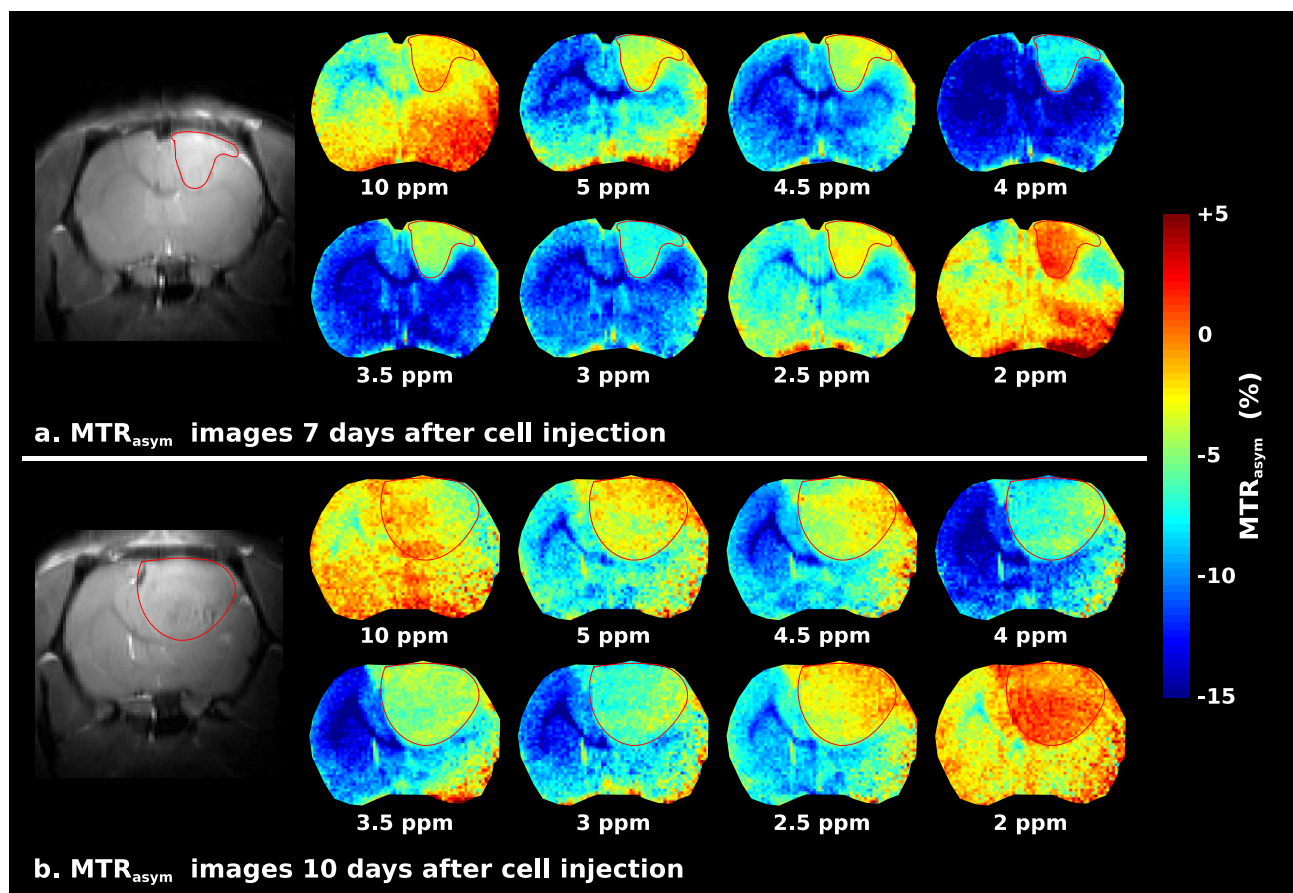


**Figure 2:** MTR<sub>asym</sub> maps obtained on a glioma-implanted rat brain using the low power ( $B_1=1.5 \mu\text{T}$ ) high-resolution CEST imaging protocol, for two different days following cell implantation. Top: 7 days after the injection of 9L glioma cells. Bottom: 11 days after the cells injection. In addition to the dominant tumor-derived features a relatively strong positive MTR<sub>asym</sub> can be observed in the lower parts of the brain for some chemical shifts, likely due to low SNR and B<sub>0</sub> inhomogeneities originating from the ear canals and the sinuses (cf. Fig. 1). Marked by the red contours are the approximate regions invaded by the glioma.

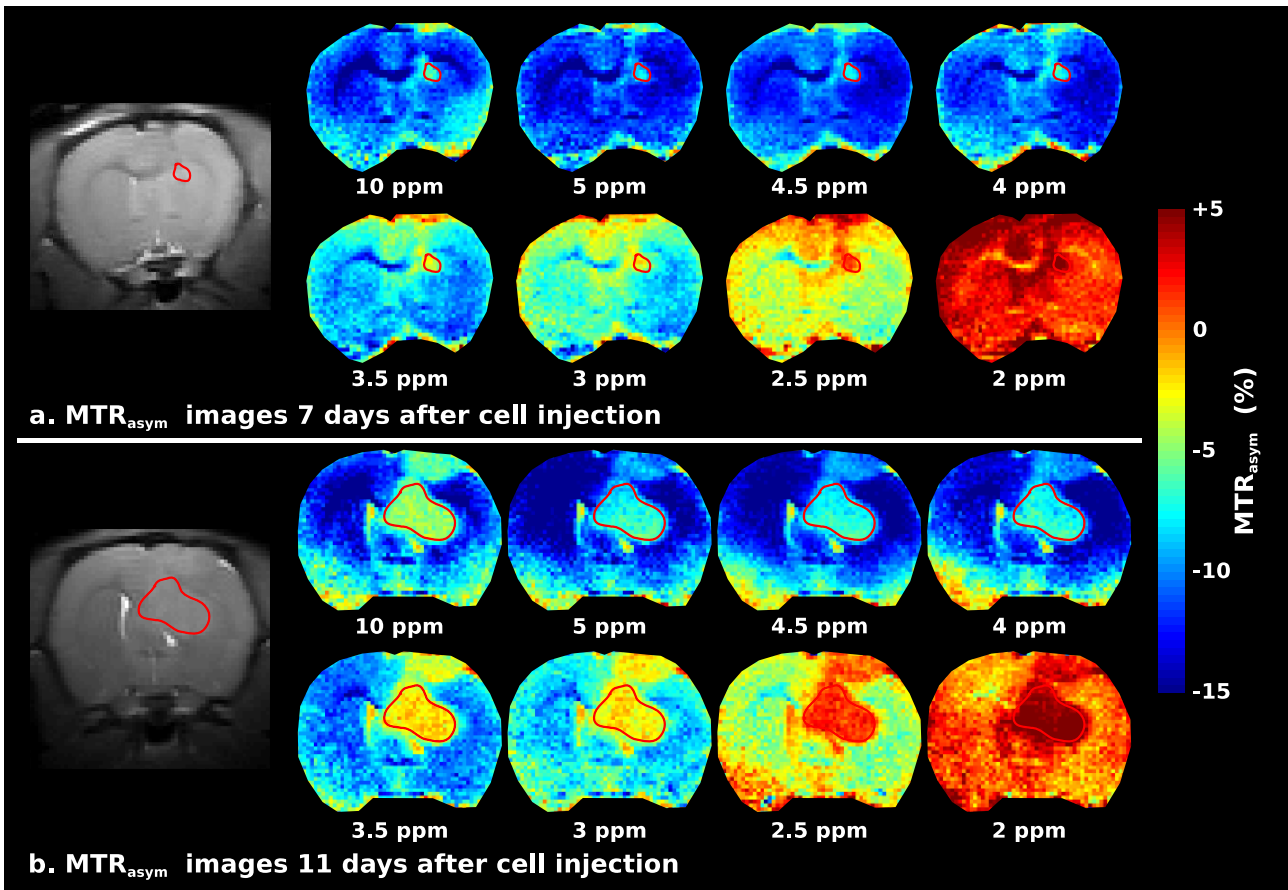


**Figure 3:**  $MTR_{asym}$  maps obtained on a glioma-implanted rat brain using the low-resolution, high-power CEST imaging protocol, for two different days following cell implantation. Top: 7 days after the injection of 9L glioma cells. Bottom: 11 days after the cells injection. The RF saturation used here was stronger ( $3.5 \mu T$ ) than that used in Figure 2, and allowed the observation of evidences an intense glioma contrast from 2.5 to 10 ppm likely originating from MT effects (red encircled regions).

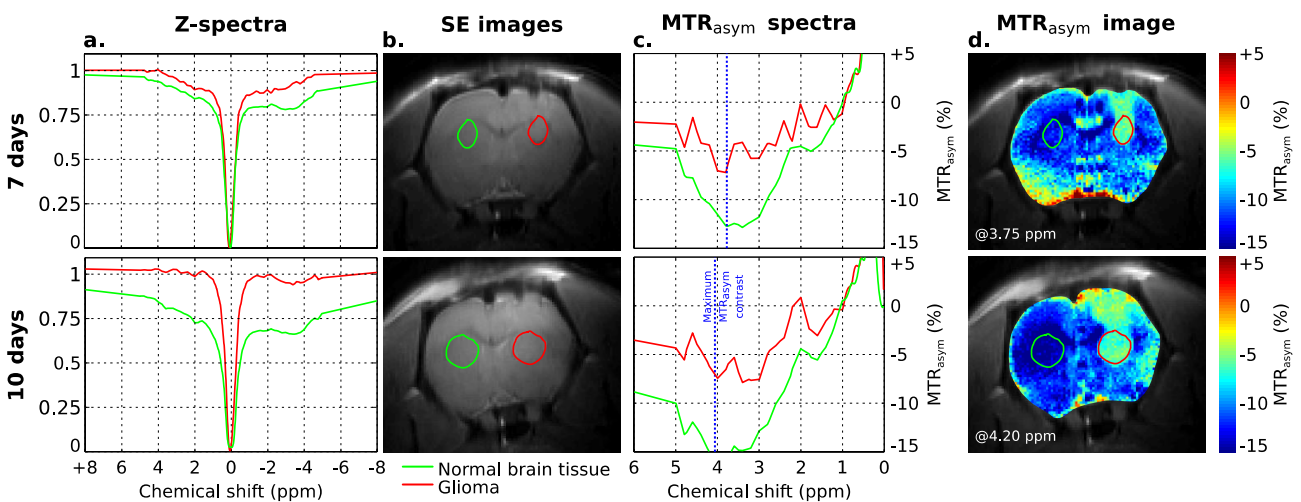


**Figure 4:** Z-spectra and  $MTR_{asym}$  maps obtained on a glioma-implanted rat for two different points in time, under low  $\gamma B_1$  saturating conditions. Top row: results observed 7 days after the 9L glioma cell injection. Bottom row: Idem but 11 days after the cell injection. (a) Anatomical RARE images showing the ROIs of normal brain and diseased regions. Notice the weak contrast between the two. (b) Localized Z-spectra extracted from normal brain (green) and glioma (red) tissues. (c) Corresponding  $MTR_{asym}$  spectra. (d)  $MTR_{asym}$  maps extracted at the chemical shift of maximum

contrast (indicated in blue in panel c) for this particular animal.

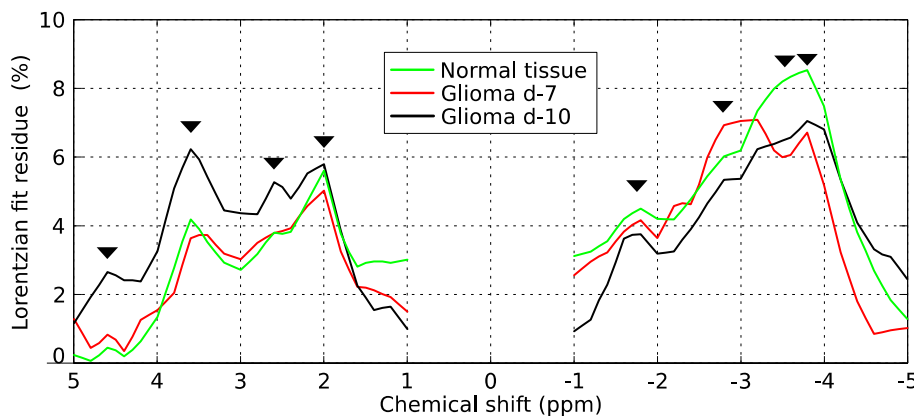
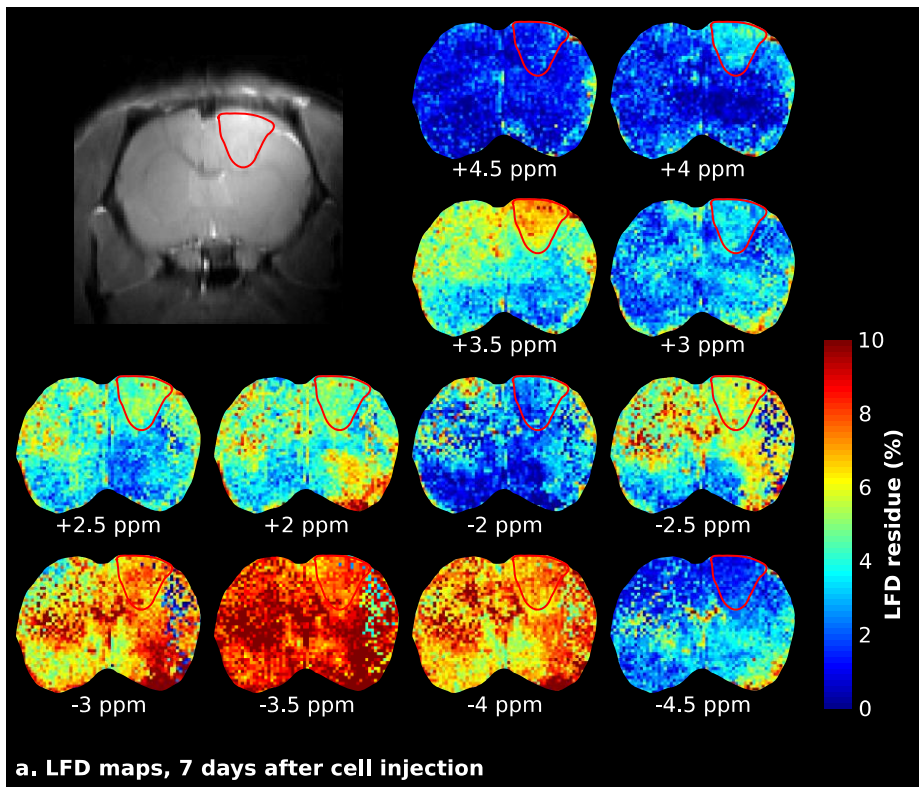


**Figure 5:** Quantitative CEST maps obtained for different saturation frequencies using the Lorentzian fit difference (LFD) method. (a) LFD maps arising on a rat bearing a day-7 glioma. Notice the strong positive contrast appearing at +3.5 ppm (APT) and the slight negative contrast observed at -3.5 ppm (NOE) for the tumorous tissue. (b) Average Z-spectra obtained using LFD over different tissues and at different stages, over the n=5 animal cohort hereby studied. The black arrows indicate multiple spectral features arising in these water-detected data at ca. -3.8 -3.5, -3.0, -1.8, +2.0, +2.6, +3.5 and +4.6 ppm, and the glioma-induced changes in these contributions as function of the days elapsed since injection. The vertical scale denotes % with respect to the maximum water signal  $S_0$ .

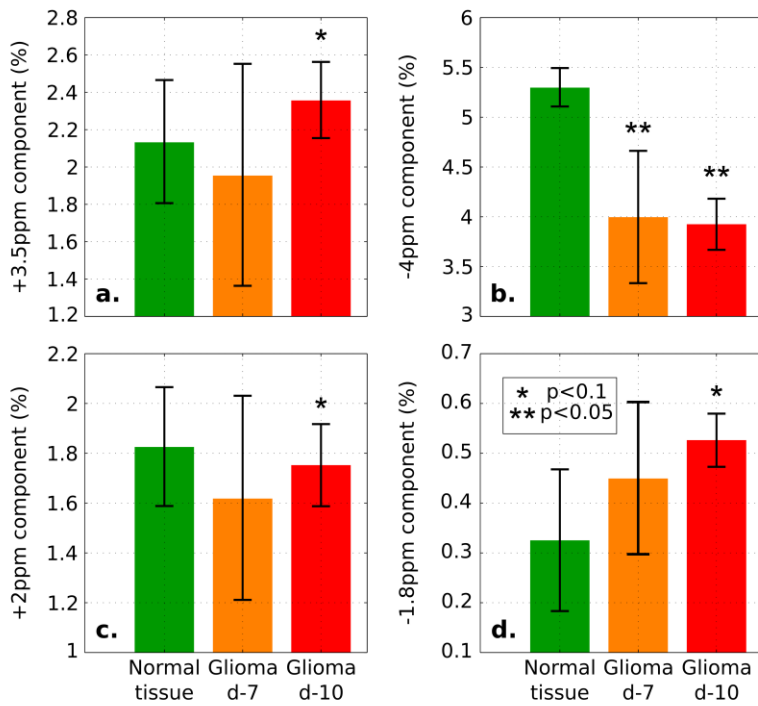


**Figure 6:** Average quantification of

the CEST contrast changes obtained using the three-offset integration technique for (a) the +3.5 ppm amide peak, (b) the NOE peak at -4 ppm, (c) the +2 amine peak, and (d) the -1.8 ppm peak., Results reflect an n=5 animal cohort. Vertical axes scales are as in Fig. 5b. Statistical significance was determined based on a paired student t-test. The error bars represent the standard error of mean (SEM) obtained over the n animals included in the group study.

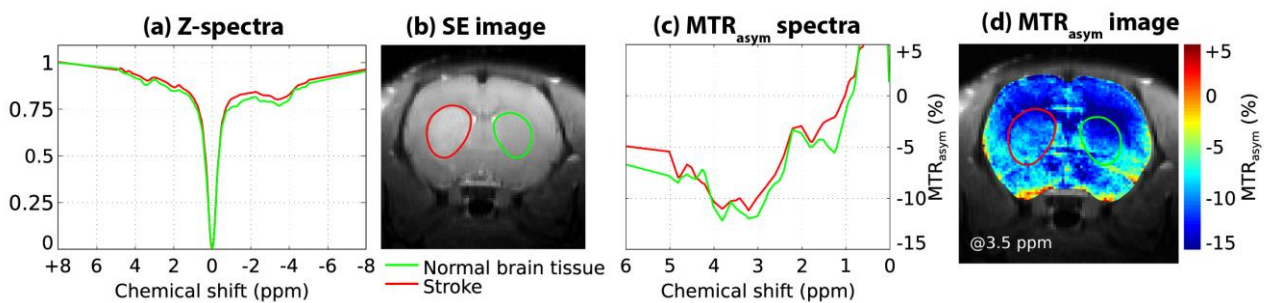


**Figure 7:** Representative CEST results obtained on a MCAO rat using the high-resolution CEST imaging protocol. (a) Anatomical RARE image illustrating the targeted ROIs. (b) Localized Z-spectra extracted from normal brain (green) and ischemic (red) brain tissues ROIs. (c) Corresponding  $MTR_{asym}$  spectra for the two ROIs. (d)  $MTR_{asym}$  map extracted for the whole organ at +3.5 ppm, i.e. close to the offset of highest  $MTR_{asym}$  for both stroked and normal regions.

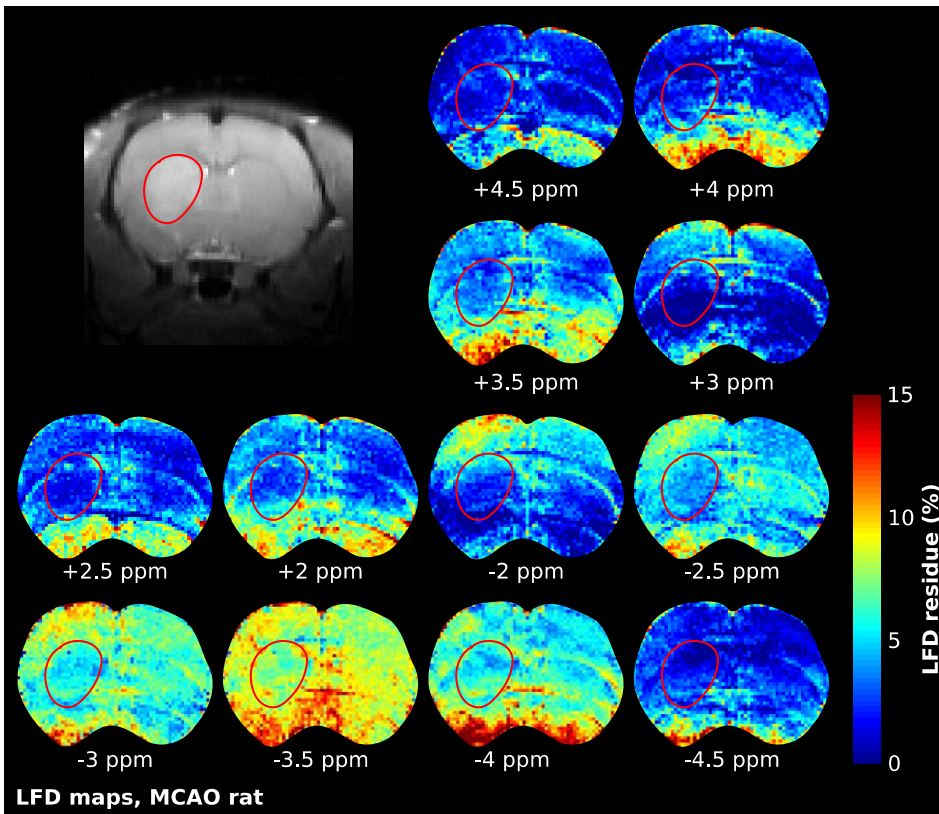
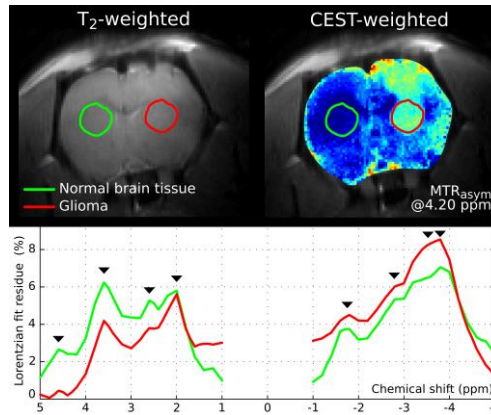


**Figure 8:** Quantitative CEST maps obtained for different saturation frequencies using the Lorentzian fit difference method on data acquired using the high-resolution CEST imaging protocol on a MCAO rat. No specific contrast could highlight the ischemic brain tissue, whose region is illustrated by the red ROI. LFD colormap scale is as in Fig. 5b.

Opportunities opened by ultrahigh field *in vivo* CEST MRI were explored, focusing on two neurological models: hypoxic ischemia and glioblastoma. A remarkably strong CEST contrast was observed at 21.1 T for the tumors, including an APT increase and a strong concurrent NOE/MT decrease. New Z-spectral features were also detected. Ischemic lesions by contrast, were more robustly detected with standard T<sub>2</sub>-weighted images than with CEST.



## Brain investigations of rodent disease models by chemical exchange saturation-transfer at 21.1 T

T. Roussel,  
J.T. Rosenberg,  
S.C. Grant and  
L. Frydman